Available online at www.sciencedirect.com
SCIENCE DIRECT®
Journal of Sound and Vibration 288 (2005) 431–462
JOURNAL OF SOUND AND VIBRATION
www.elsevier.com/locate/jsvi

A fuzzy finite element procedure for the calculation of uncertain frequency-response functions of damped structures: Part 1—Procedure

David Moens*, Dirk Vandepitte

K.U. Leuven, Department of Mechanical Engineering, PMA, Celestijnenlaan 300B, B-3001 Heverlee, Belgium

Received 22 April 2004; accepted 5 July 2005
Available online 22 August 2005

Abstract

This work introduces a numerical algorithm to calculate frequency-response functions (FRFs) of damped finite element (FE) models with fuzzy uncertain parameters. Part one of this paper describes the numerical algorithm for the solution of the underlying interval finite element (IFE) problem. First, the IFE procedure for the calculation of undamped envelope FRFs is discussed. Starting from the undamped procedure, a strategy is developed to analyse damped structures based on the principle of Rayleigh damping. This is achieved by analysing the effect of the proportional damping coefficients on the subsequent steps of the undamped procedure. This finally results in a procedure for the calculation of fuzzy damped FRFs based on an analytical extension of the undamped algorithm. Part one of this paper introduces the numerical procedure. Part two of this paper illustrates the application of the methodology on four numerical case studies.

1. Introduction

The current status of numerical analysis tools enables a very precise simulation of physical phenomena using a virtual numerical model. The broad applicability of numerical techniques in combination with their very limited cost, have initiated an exponential increase of their use in the

*Corresponding author.
E-mail address: david.moens@mech.kuleuven.be (D. Moens).

0022-460X/$ - see front matter © 2005 Elsevier Ltd. All rights reserved.
doi:10.1016/j.jsv.2005.07.001

design of new products. Consequently, the *virtual prototyping* phase has evolved to a substantial part of modern design processes. Especially, the finite element (FE) method has become a very popular tool for design validation and optimisation.

Nowadays, the computational capabilities of modern computers causes an evolution towards the use of extremely detailed numerical models. While these models theoretically enable the simulation of the vast majority of relevant physical processes, they also require a large amount of numerical input data in order to describe the model and all of its details realistically. This means that it becomes harder to ensure a general reliability of the detailed models, and consequently, of the outcome of the numerical analyses based on these models. It is more and more acknowledged that, in order to perform a trustworthy design validation based on such models, the computational power could be of greater benefit when it is used for the inclusion of uncertainties in the numerical model rather than for modelling all deterministic details. Furthermore, through the inclusion of non-deterministic aspects, the numerical analysis will come closer to a description of the actual behaviour of the modelled product since uncertainty and variability are inherent to production processes.

Over the past decades, a number of methodologies have been developed that include uncertain model properties in the FE analysis and aim at the quantification of the uncertainty on the analysis result. The probabilistic concept is by far the most popular for numerical uncertainty modelling. Its popularity has lead to a number of probabilistic FE procedures [1,2]. These procedures are becoming increasingly popular, mainly due to their ease of use. However, there is a growing awareness that non-deterministic properties cannot always be exactly represented using the probabilistic concept. An actual *variability*, i.e., a property which will vary in the actual product, is often not completely predictable, which leads to the introduction of assumptions concerning its probabilistic description. On the other hand, some properties of the model which are invariable in the actual product could be unknown or unspecified in an early design stage. These are often referred to as *uncertainties* (see also Ref. [3] or the second part of this paper for a clear description of variability and uncertainty). The probabilistic model in this case represents personal opinion or preference of the designer rather than actual variability. In both cases, the probabilistic model does not give an objective description of reality. Furthermore, a mixture of both fundamentally different interpretations in a single probabilistic analysis might lead to subjective or misleading conclusions. But next to these theoretical objections, there is also a practical limitation associated with probabilistic analysis. The most popular implementation of probabilistic numerical analysis is the Monte Carlo simulation [4]. This technique requires a large number of deterministic calculations, and is therefore limited in its applicability when realistic industrially sized models are analysed.

The inevitable presence of uncertainties and unpredictable variabilities in an early design stage has initiated research activities towards non-probabilistic approaches for numerical uncertainty analysis (see Ref. [5] for a more extensive description of the current status of non-probabilistic approaches for uncertainty treatment in FE analysis). One of the most basic non-probabilistic approaches is the interval finite element (IFE) method. Based on the interval concept, the non-deterministic model properties are defined using a range between a lower and an upper bound. Values outside this range are considered to be strictly impossible. The aim of the IFE procedure is to calculate the range of possible analysis results taking into account all possible combinations of the uncertain inputs within their allowable range. There have been some attempts to develop

numerical algorithms for IFE analysis in specific domains [6–8]. Up to now, however, there exists no generally applicable IFE procedure. Furthermore, a general criticism on the IFE procedure often stated in literature refers to the problem of dependency within interval arithmetic. The fact that parameter dependencies are lost throughout the interval procedure causes an artificial overestimation in each step of the interval algorithm, which can lead to an undesirably high amount of conservatism in the final IFE analysis result. This is explained in more detail in Section 2.3. Also in this section, a remedy for this conservatism is introduced, based on a hybrid optimisation-interval arithmetic procedure.

The IFE method requires the specification of strict bounds on all non-deterministic model properties. These bounds may be subject to uncertainty. In order to analyse the influence of these boundaries on the analysis results, a fuzzy finite element (FFE) method has been developed [9–12]. This paper briefly describes the main principle and some computational aspects of this method in Section 2. In the following sections, the application of FFEM to frequency-response function (FRF) analysis is described. Section 3 first summarises the undamped procedure. This procedure is extended to proportionally damped models in Section 4.

2. The fuzzy finite element method

2.1. Fuzzy uncertainty modelling

The theory of fuzzy logic was introduced by Zadeh [13] in 1965, and has gained an increasing popularity during the last two decades. Its most important property is that it is capable of describing linguistic and therefore incomplete information in a non-probabilistic manner. This is achieved using the concept of fuzzy sets. A fuzzy set can be interpreted as an extension of a classical set. Where a classical set clearly distinguishes between members and non-members of the set, the fuzzy set introduces a degree of membership, represented by the *membership function*. For a fuzzy set $\tilde{x}$, the membership function is defined as $\mu_{\tilde{x}}(x)$ for all x that belong to the domain X

$$\tilde{x} = \{(x, \mu_{\tilde{x}}(x)) \mid (x \in X)(\mu_{\tilde{x}}(x) \in [0, 1])\}. \tag{1}$$

This membership function describes the grade of membership to the fuzzy set for each element in the domain. If $\mu_{\tilde{x}}(x) = 1$, x is definitely a member of the subset $\tilde{x}$. If $\mu_{\tilde{x}}(x) = 0$, x is definitely not a member of the subset $\tilde{x}$. Opposed to the interval concept, fuzzy sets allow membership values different from zero and one. For every x with $0 < \mu_{\tilde{x}}(x) < 1$, the membership is not certain. This enables the representation of a value that is only to a certain degree member of the set.

2.2. Fuzzy arithmetic

Working with fuzzy numbers in a numerical context first requires a convention on how to handle the combination of fuzzy numbers. For this purpose, an appropriate t-norm has to be chosen. This work applies the t-min norm, which is by far the most widely adopted t-norm in fuzzy numerical analysis. Its main benefit is that by applying the t-min norm within the extension principle [14], the numerical result of a combination of fuzzy variables can be calculated using the α-sublevel technique (see Ref. [5] for a proof). This technique subdivides the membership range

into a number of α-levels. The intersection with the membership function of the input uncertainties at each level results in an interval. With these input intervals of the α-sublevel, an interval analysis corresponding to the deterministic analysis is performed. This results in an interval for the analysis result at the considered α-level. Finally, the fuzzy solution is assembled from the resulting intervals at each sublevel, repeating this procedure for a number of α-sublevels. Fig. 1 clarifies this procedure for a function of two triangular fuzzy variables.

The core problem of this procedure is the calculation of the result of the function in interval arithmetic. An interval is denoted by $x^I = [\underline{x}, \overline{x}]$. For a function of n fuzzy variables $f(\tilde{x}_1, \tilde{x}_2, \ldots, \tilde{x}_n)$, the result is calculated at each α-sublevel from the solution set defined as

$$y_\alpha^I = \{y \mid (\exists x_i \in x_{i\,\alpha}^I, \forall i = 1, \ldots, n)(y = f(x_1, x_2, \ldots, x_n))\} \tag{2}$$

with $x_{i\,\alpha}^I$ describing the interval of the fuzzy variable $\tilde{x}_i$ at level α. This technique guarantees a constant size of the data set during computation. Another advantage is that the calculation of a fuzzy function can be optimised to a trade-off between computational effort and correctness by selecting the number of α-sublevels.

2.3. Fuzzy finite element analysis

The FFE method as introduced by Chen [10] consists of the application of the α-sublevel strategy on the numerical procedure of the deterministic FE analysis. From the previous section it is clear that the solution of the interval problem corresponding to the FE analysis is the numerical core of the method. Consider the interval vector $\mathbf{x}^I$ of uncertain input parameters of the FE model, referred to as the interval input parameter space. The interval solution requires a procedure to calculate the range of possible FE analysis outcomes, given that all input parameters

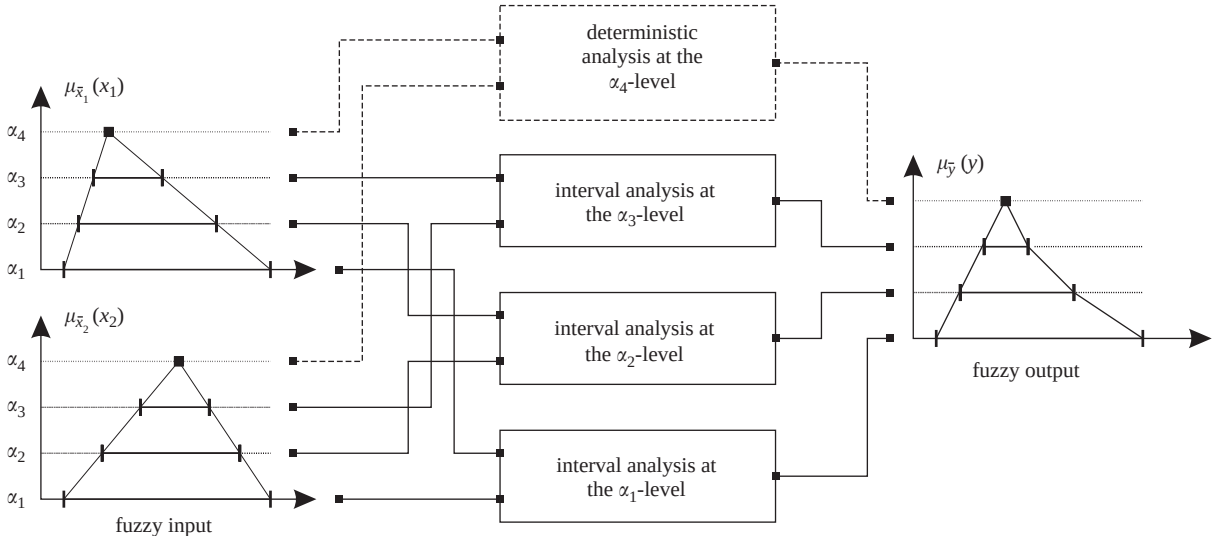

Fig. 1. Scheme of the numerical procedure to perform a fuzzy FE analysis using 4 α-sublevels.

are within the interval input parameter space. A number of concepts have been developed for this purpose. In the most commonly applied interval arithmetical approach, the total deterministic FE procedure is translated to interval arithmetic using the interval counterparts of all basic operations. The resulting procedure generally consists of two steps:

1. the translation of the interval input parameter space to an interval system description based on interval system matrices,
2. the approximation of the solution of the analysis expressed as an interval problem using the interval system matrices.

The assembly of the interval system matrices in the first step results from the translation of the deterministic assembly procedure to interval analysis. It has been shown [5] that this step generally introduces conservatism, since dependency between different elements of the model through common interval parameters are lost in the assembly. Furthermore, the system interval matrix does not model the dependencies between the elements of the matrix itself, and loses as such important information on internal matrix correlations. The resulting interval matrices therefore implicitly incorporate artificial matrices in the analysis, which are not feasible using the physical FE model. For realistic industrially sized FE models, this conservatism could render the rest of the analysis little useful.

A new efficient calculation strategy that remedies the excessive conservatism was introduced by the authors [5]. It is a hybrid procedure, consisting of both a global optimisation and an interval arithmetic part. In the first part, an optimisation is applied to calculate the exact interval result at some intermediate step of the total algorithm. This is achieved by minimising and maximising the intermediate results over the interval input parameter space. In the second part, the interval arithmetical procedure is applied on these intermediate interval results. The main advantage of this method is that all conservatism prior to the optimised intermediate results is neutralised.

This approach has been successfully applied in an IFE procedure for the calculation of undamped interval FRFs [15]. In the first part of this procedure, the optimisation is used to translate the interval input parameter space to the exact ranges of the modal stiffness and mass parameters of the structure. The calculation of the envelope FRFs in the second part is done by applying the interval arithmetic equivalent of the modal superposition procedure on these interval modal parameters. This procedure neutralises all conservatism in the matrix assembly phase, since it directly uses the modal parameters as goal functions in the optimisation part. In order to extend this procedure to damped structures, Section 3 now first summarises this procedure for undamped structures.

3. Interval procedure for undamped frequency-response function analysis

In the remainder of this paper, a set is denoted by x^S. A set generally consists of the union of a number of interval objects. The range of a function $f(x)$ taking into account all possible values of the function variable x inside a set x^S is denoted by $\langle f \rangle_{x^S}$.

3.1. Interval response analysis based on modal superposition

The deterministic modal superposition concept states that, considering the first n modes, the FRF between node j and k equals

$$\mathrm{FRF}_{jk} = \sum_{i=1}^{n} \frac{\Phi_{i_k}\Phi_{i_j}}{\boldsymbol{\Phi}_i^{\mathrm{T}}\mathbf{K}\boldsymbol{\Phi}_i - \omega^2\boldsymbol{\Phi}_i^{\mathrm{T}}\mathbf{M}\boldsymbol{\Phi}_i} \tag{3}$$

with $\boldsymbol{\Phi}_i$ the ith eigenvector of the system. Simplification of Eq. (3) yields

$$\mathrm{FRF}_{jk} = \sum_{i=1}^{n} \frac{1}{\hat{k}_i - \omega^2\hat{m}_i} \tag{4}$$

with $\hat{k}_i$ and $\hat{m}_i$ the normalised modal parameters

$$\hat{k}_i = \frac{\boldsymbol{\Phi}_i^{\mathrm{T}}\mathbf{K}\boldsymbol{\Phi}_i}{\Phi_{i_j}\Phi_{i_k}}, \tag{5}$$

$$\hat{m}_i = \frac{\boldsymbol{\Phi}_i^{\mathrm{T}}\mathbf{M}\boldsymbol{\Phi}_i}{\Phi_{i_j}\Phi_{i_k}}. \tag{6}$$

Fig. 2(a) gives a graphical overview of this deterministic modal superposition procedure. It introduces the function $\mathscr{D}(\omega) = (\hat{k}_i - \omega^2\hat{m}_i)$ to express the modal response denominator as a function of the frequency. The corresponding IFE procedure results from a step by step set

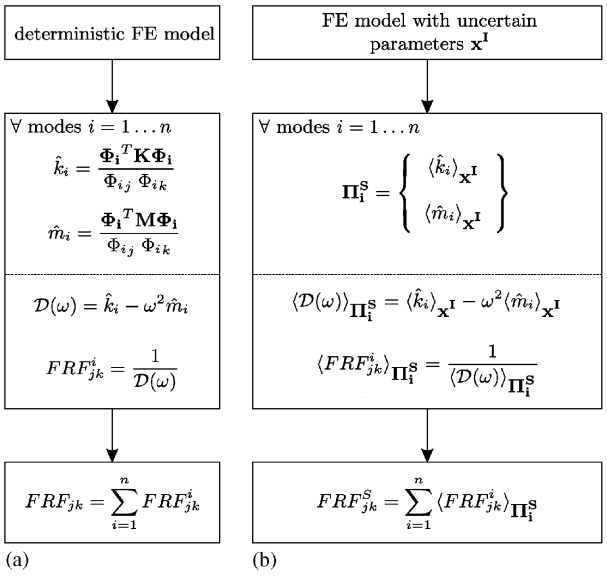

Fig. 2. Translation of the deterministic modal superposition algorithm to an equivalent IFE procedure: (a) deterministic algorithm and (b) set translated algorithm.

translation of this algorithm, as illustrated in Fig. 2(b). This shows that the total envelope FRF can be calculated in three principal steps:

1. for each mode, the translation of the interval input parameter space $\mathbf{x}^I$ to the modal parameter space, resulting in the modal parameters ranges $\langle \hat{k}_i \rangle_{\mathbf{x}^I}$ and $\langle \hat{m}_i \rangle_{\mathbf{x}^I}$, which are combined in the modal parameter set vector $\mathbf{\Pi}_i^S$,
2. for each mode, the calculation of the modal envelope FRF by substitution of the ranges of the modal parameters in the denominator function $\mathscr{D}(\omega)$, and subsequently inverting the resulting denominator function range,
3. the summation of the individual envelope FRFs of all modes.

Steps 1 and 2 should be performed for each mode that is taken into account in the modal superposition. Using this procedure, the computational cost is controllable by selecting only the modes which contribute to the total FRF in the frequency domain of interest.

The modal parameter ranges in the first step of the procedure are calculated through a global optimisation. By considering the modal parameters as direct functions of the uncertain model properties $\mathbf{x}$, their exact ranges can be calculated by performing a minimisation and a maximisation over the interval input space. In the most straightforward implementation, the ranges of both modal parameters are considered independently from one another. This results in the *Modal Rectangle method* (MR). However, it is clear that the modal stiffness and mass of a particular mode are coupled through the modal vector components of the considered FE model. This means that the MR method can be improved by incorporating this dependency between the modal parameters. This is achieved using the *Modal Rectangle method with Eigenvalue interval correction* (MRE). The MR and MRE method are described more in detail in Sections 3.2 and 3.3, respectively, using the basic three-step procedure described above.

3.2. The modal rectangle method

This procedure is based on a graphical interpretation in the modal parameter space. Each step will refer to this graphical interpretation.

3.2.1. MR method, step 1

The first part of the MR procedure consists of the derivation of the ranges of the modal parameters of each mode taking into account the complete interval input parameters space. Theoretically, the modal parameters are fully coupled through the global system, and the exact range of a mode's modal parameter pairs equals:

$$\langle \hat{k}_i, \hat{m}_i \rangle = \{(\hat{k}_i, \hat{m}_i) \mid (\mathbf{x} \in \mathbf{x}^I)\}. \tag{7}$$

The grey area in Fig. 3 represents a possible $\langle \hat{k}_i, \hat{m}_i \rangle$-domain.

In the MR method, the coupling between the modal stiffness and mass is neglected. This means that the modal parameter ranges are considered as mathematically independent entities:

$$\langle \hat{k}_i \rangle_{\mathbf{x}^I} = \left\{ \hat{k}_i \mid (\mathbf{x} \in \mathbf{x}^I) \left(\hat{k}_i = \frac{\mathbf{\Phi}_i^{\mathrm{T}} \mathbf{K} \mathbf{\Phi}_i}{\Phi_{i_j} \Phi_{i_k}} \right) \right\}, \tag{8}$$

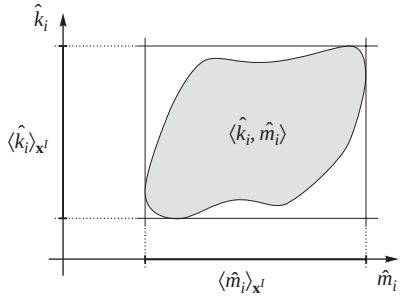

Fig. 3. Graphical illustration of a mode's $\langle \hat{k}_i, \hat{m}_i \rangle$-domain and its approximation using the modal rectangle method.

$$\langle \hat{m}_i \rangle_{\mathbf{x}^I} = \left\{ \hat{m}_i \mid (\mathbf{x} \in \mathbf{x}^I) \left(\hat{m}_i = \frac{\boldsymbol{\Phi}_i^{\mathrm{T}} \mathbf{M} \boldsymbol{\Phi}_i}{\Phi_{i_j} \, \Phi_{i_k}} \right) \right\}. \tag{9}$$

Graphically, this means that the $\langle \hat{k}_i, \hat{m}_i \rangle$-domain of Fig. 3 is approximated by a conservative rectangle as indicated in the figure. The most straightforward numerical implementation would be to calculate the bounds on the modal parameter ranges by minimising and maximising the modal parameters over the interval input parameter space. However, the denominator of the modal parameters defined in Eqs. (5) and (6) possibly equals zero. This will cause the optimisation to fail. This problem is avoided by defining the inverse of the modal parameters expressed as $\hat{k}_i^{-1}$ and $\hat{m}_i^{-1}$ as goal functions for the optimisation. The resulting ranges $\langle \hat{k}_i^{-1} \rangle_{\mathbf{x}^I}$ and $\langle \hat{m}_i^{-1} \rangle_{\mathbf{x}^I}$ can be proved to be single continuous intervals. Furthermore, in many practical situations, the inverted modal parameters are monotonic functions of the input properties, which generally leads to a fast convergence in the optimisation procedure.

Using $\hat{k}_i^{-1}$ and $\hat{m}_i^{-1}$ as goal functions, the modal parameter ranges are calculated from the inversion of the intervals between the optimisation results. Based on the signs of these optimised interval bounds, two different situations can occur. In the most general case, both the optimised lower and upper bound have the same sign. Based on Eqs. (8) and (9), it can be seen that in this case, after the inversion, the modal stiffness and the modal mass parameter range always have the same sign. Therefore, the resulting $\langle \hat{k}_i, \hat{m}_i \rangle$-domain approximation is situated either in the first or in the third quadrant of the modal parameter space. The corresponding modes are referred to as respectively *positive modes* and *negative modes*. The second situation occurs when the calculated interval on the inversed modal parameters ranges over zero. In this case, the Kahan inversion [16] is applied. This is an extension of the classical interval division that defines the result of the inversion of an interval over zero to equal the union of two intervals ranging from a finite value to infinity, respectively, in the negative and positive range of real numbers. The modal rectangle in this case consists of two semi-infinite regions in the first and third quadrant of the modal parameter space, and the modes are referred to as *switch modes*.

Leaving switch modes out of this discussion, the first step of the MR procedure results in the description of the modal parameter ranges of the modes taken into account in the modal superposition

$$\langle \hat{k}_i \rangle_{\mathbf{x}^I} = \left[\frac{1}{\overline{\hat{k}_i^{-1}}}, \frac{1}{\underline{\hat{k}_i}^{-1}} \right] = [\underline{\hat{k}_i}, \overline{\hat{k}_i}], \tag{10}$$

$$\langle \hat{m}_i \rangle_{\mathbf{x}^I} = \left[\frac{1}{\overline{\hat{m}_i^{-1}}}, \frac{1}{\underline{\hat{m}_i^{-1}}} \right] = [\underline{\hat{m}_i}, \overline{\hat{m}_i}]. \tag{11}$$

For the further development of the algorithm, the modal parameter ranges are combined in a set vector for each mode

$$\mathbf{\Pi}_i^S = \left\{ \begin{array}{c} \langle \hat{k}_i \rangle_{\mathbf{x}^I} \\ \langle \hat{m}_i \rangle_{\mathbf{x}^I} \end{array} \right\}. \tag{12}$$

3.2.2. MR method, step 2

In the second step of the MR procedure, the modal envelope FRF for each mode's contribution is calculated. The requested output of this step of the algorithm is the modal envelope FRF, expressed as the range of the modal response function FRF_{jk}^i taking into account the range of the modal parameters in the vector $\mathbf{\Pi}_i^S$

$$\langle \mathrm{FRF}_{jk}^i \rangle_{\mathbf{\Pi}_i^S} = \left\{ \frac{1}{\hat{k}_i - \omega^2 \hat{m}_i} \mid (\hat{k}_i \in \langle \hat{k}_i \rangle_{\mathbf{x}^I})(\hat{m}_i \in \langle \hat{m}_i \rangle_{\mathbf{x}^I}) \right\}. \tag{13}$$

The procedure first calculates the envelope of the modal denominator function $\mathscr{D}(\omega)$, after which this envelope is inverted. Graphically, the denominator function $\hat{k}_i - \omega^2 \hat{m}_i = \mathscr{D}^*$ represents a straight line in the $(\hat{k}_i, \hat{m}_i)$-space. All $\hat{k}_i, \hat{m}_i$-pairs on this line represent structures with equal values $\mathscr{D}^*$ for the modal FRF denominator function. This value is graphically equivalent with the ordinate of the intersection of the line and the $\hat{k}_i$-axis. This is illustrated in Fig. 4. Using this graphical interpretation, the exact range of the modal FRF denominator function $\langle \mathscr{D}(\omega) \rangle_{\mathbf{x}^I}$ follows from constructing both lines with a slope ω^2 tangent to the exact $\langle \hat{k}_i, \hat{m}_i \rangle$-domain, as illustrated in Fig. 5. However, since the exact $\langle \hat{k}_i, \hat{m}_i \rangle$-domain is unknown, the denominator function range has to be approximated using the MR $\langle \hat{k}_i, \hat{m}_i \rangle$-domain approximation. This is done using the upper left and lower right corner of the rectangular approximation as also indicated in Fig. 5.

Numerically, the MR approximation of the denominator function range equals

$$\langle \mathscr{D}(\omega) \rangle_{\mathbf{\Pi}_i^S} = [\underline{\hat{k}_i} - \omega^2 \overline{\hat{m}_i}, \overline{\hat{k}_i} - \omega^2 \underline{\hat{m}_i}]. \tag{14}$$

This function range is graphically illustrated in Fig. 6(a). From this figure, it is clear that the modal denominator function range is an interval for every frequency in the frequency domain.

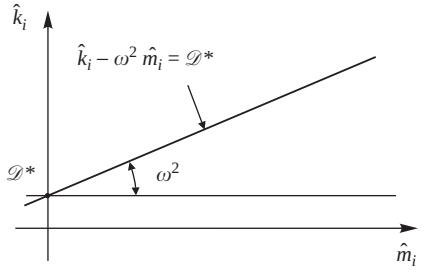

Fig. 4. Graphical interpretation of the modal denominator function in the modal space.

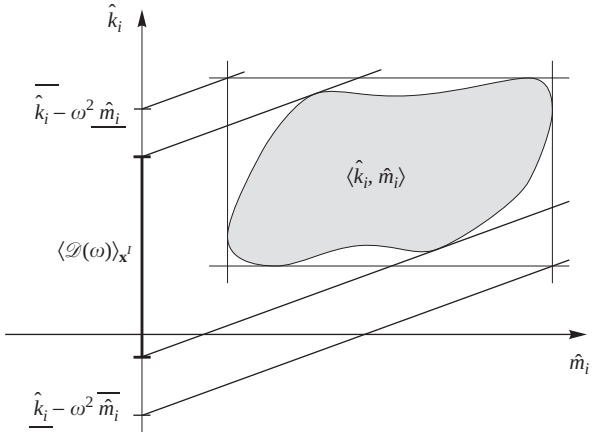

Fig. 5. Conservatism in the modal FRF denominator function range calculation using the modal rectangle method.

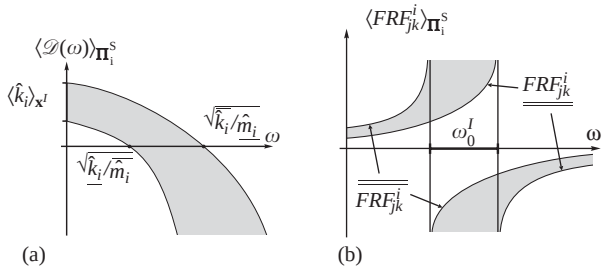

Fig. 6. Modal denominator function range and FRF envelope using the MR strategy: (a) denominator function range and (b) modal envelope FRF.

This interval contains zero for frequencies within the interval

$$\omega_0^I = \left[\sqrt{\underline{\hat{k}_i}/\overline{\hat{m}_i}}, \sqrt{\overline{\hat{k}_i}/\underline{\hat{m}_i}} \right]. \tag{15}$$

This means that the Kahan inversion is required to invert the modal FRF denominator function range of Eq. (14) for frequencies inside the ω_0^I interval. This finally results in

$$\langle \mathrm{FRF}_{jk}^i \rangle_{\mathbf{\Pi}_i^S} = \begin{cases} \left[\underline{\underline{\mathrm{FRF}_{jk}^i}} \; \overline{\overline{\mathrm{FRF}_{jk}^i}} \right] & \forall\, \omega \notin \omega_0^I, \\ \left[-\infty \overline{\overline{\mathrm{FRF}_{jk}^i}} \right] \cup \left[\underline{\underline{\mathrm{FRF}_{jk}^i}} +\infty \right] & \forall\, \omega \in \omega_0^I \end{cases} \tag{16}$$

with

$$\underline{\underline{\mathrm{FRF}_{jk}^i}} = \frac{1}{\overline{\hat{k}_i} - \omega^2 \underline{\hat{m}_i}}, \tag{17}$$

$$\overline{\overline{\mathrm{FRF}_{jk}^{i}}} = \frac{1}{\underline{\hat{k}_i} - \omega^2 \overline{\hat{m}_i}}. \tag{18}$$

Fig. 6(b) illustrates the result of the inversion the denominator function range in the frequency domain.

3.2.3. MR method, step 3

The final step for the computation of the total envelope FRF consists of the summation of all modal envelope FRFs. As indicated in Eq. (16), the response range differs for frequencies within and outside the ω_0^I interval. Therefore, the summation distinguishes between three sub cases

- for frequencies outside the ω_0^I interval of every mode, the range of all terms in the summation is an interval. At these frequencies, the range of the total FRF equals

$$\mathrm{FRF}_{jk}^{S} = \left[\sum_{i=1}^{n} \underline{\underline{\mathrm{FRF}_{jk}^{i}}}, \sum_{i=1}^{n} \overline{\overline{\mathrm{FRF}_{jk}^{i}}} \right] \tag{19}$$

- for frequencies inside exactly one ω_0^I interval, one term in the summation is the union of two disjoint intervals over infinity. At these frequencies, the range of the total FRF equals

$$\mathrm{FRF}_{jk}^{S} = \left[-\infty, \sum_{i=1}^{n} \overline{\overline{\mathrm{FRF}_{jk}^{i}}} \right] \cup \left[\sum_{i=1}^{n} \underline{\underline{\mathrm{FRF}_{jk}^{i}}}, +\infty \right] \tag{20}$$

- for frequencies inside overlapping ω_0^I intervals, two or more terms are the union of two disjoint intervals over infinity. At these frequencies, the range of the total FRF equals

$$\mathrm{FRF}_{jk}^{S} = [-\infty, +\infty]. \tag{21}$$

The conversion of the finally obtained envelope FRF into an envelope on the amplitude of the FRF is trivial.

3.3. The modal rectangle method with eigenvalue interval correction

The enhancement in this procedure can be understood best in the graphical interpretation in the modal parameter space. For the sake of briefness, the corresponding analytical derivation of all the equations in the algorithm is not given in this paper, as it can be found in Ref. [15].

From Fig. 5 it is clear that combining the independently calculated modal parameter ranges to a conservative rectangle around the exact $\langle \hat{k}_i, \hat{m}_i \rangle$-domain introduces conservatism in the modal denominator function range approximation, and consequently in the modal envelope FRFs. The amount of conservatism will be substantial when the shape of the exact modal domain differs thoroughly from the approximate rectangle. A possible strategy to reduce this conservatism is to use a better approximation of the exact $\langle \hat{k}_i, \hat{m}_i \rangle$-domain. This is achieved by introducing the exact eigenvalue intervals into the analysis.

Based on the fact that an eigenvalue λ_i equals the quotient of the modal parameters $\hat{k}_i$ and $\hat{m}_i$, it is clear that an eigenvalue interval λ_i^I introduces an extra restriction on the set of possible combinations of the modal parameters

$$\underline{\lambda_i} \leqslant \frac{\hat{k}_i}{\hat{m}_i} \leqslant \overline{\lambda_i}. \tag{22}$$

In order to use this extra restriction in the MR procedure, the eigenvalue interval λ_i^I should equal the exact range of the eigenvalue with respect to the interval input parameter space $\langle \lambda_i \rangle_{\mathbf{x}^I}$. Similar to the calculation of the modal parameter ranges in the MR procedure, these can be calculated through a global optimisation on the eigenvalues over the input interval space. The enhancement resulting from this extra restriction is expressed in the redefinition of the modal envelope FRF of Eq. (13) by adding the eigenvalue interval to the conditions of the set definition

$$\langle \mathrm{FRF}_{jk}^i \rangle_{\mathbf{\Gamma}_i^S} = \left\{ \frac{1}{\hat{k}_i - \omega^2 \hat{m}_i} \mid (\mathbf{\Pi}_i \in \mathbf{\Pi}_i^S) \left(\frac{\hat{k}_i}{\hat{m}_i} \in \langle \lambda_i \rangle_{\mathbf{x}^I} \right) \right\} \tag{23}$$

with

$$\mathbf{\Gamma}_i^S = \left\{ \begin{array}{c} \mathbf{\Pi}_i^S \\ \langle \lambda_i \rangle_{\mathbf{x}^I} \end{array} \right\}. \tag{24}$$

Graphically, the eigenvalue bounds represent lines with the minimal and maximal possible slope through the origin of the $(\hat{k}_i, \hat{m}_i)$-space. These lines are extra delimiters for the $\langle \hat{k}_i, \hat{m}_i \rangle$-domain approximation as illustrated in Fig. 7.

Using the graphical interpretation as in Fig. 5, the approximate modal FRF denominator function range is derived constructing lines tangent to the new $\langle \hat{k}_i, \hat{m}_i \rangle$-domain approximation. In this case these lines pass through the corner points of the polygonal $\langle \hat{k}_i, \hat{m}_i \rangle$-domain approximation indicated with triangles in the figure. The approximation of the upper bound of the modal FRF denominator function range uses c_1 for $\omega^2 \leqslant \overline{\lambda_i}$ and c_2 for $\omega^2 \geqslant \overline{\lambda_i}$, and the lower

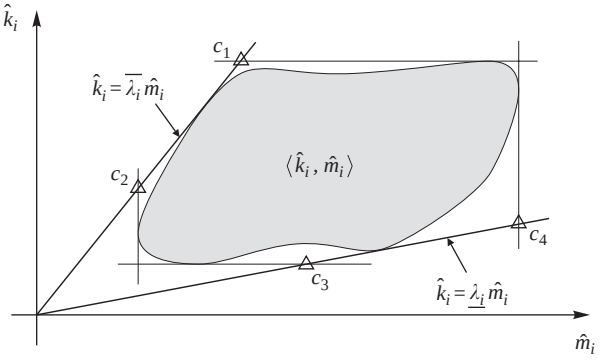

Fig. 7. Effect of the introduction of the exact eigenvalue interval in the $\langle \hat{k}_i, \hat{m}_i \rangle$-domain approximation of a positive mode.

bound uses c_3 for $\omega^2 \leqslant \underline{\lambda_i}$ and c_4 for $\omega^2 \geqslant \underline{\lambda_i}$. This results in the following analytical expressions:

$$\langle \mathscr{D}(\omega) \rangle_{\mathbf{\Gamma}_i^S} = \begin{cases} \left[\underline{\hat{k}_i}\left(1 - \dfrac{\omega^2}{\underline{\lambda_i}}\right), \overline{\hat{k}_i}\left(1 - \dfrac{\omega^2}{\overline{\lambda_i}}\right) \right] & \text{for } \omega^2 \leqslant \underline{\lambda_i}, \\ \left[\overline{\hat{m}_i}(\underline{\lambda_i} - \omega^2), \overline{\hat{k}_i}\left(1 - \dfrac{\omega^2}{\overline{\lambda_i}}\right) \right] & \text{for } \underline{\lambda_i} < \omega^2 < \overline{\lambda_i}, \\ [\overline{\hat{m}_i}(\underline{\lambda_i} - \omega^2), \underline{\hat{m}_i}(\overline{\lambda_i} - \omega^2)] & \text{for } \overline{\lambda_i} \leqslant \omega^2. \end{cases} \tag{25}$$

Fig. 8 illustrates the modal FRF denominator function range approximation using the MRE approach. By introducing the exact eigenvalue intervals, the ω_0^I domain now is narrowed to the actual eigenfrequency range. This results in a substantial decrease of the width of the function range compared to the MR method, as also illustrated in Fig. 8.

Finally, the modal envelope FRF results from the inversion of the enhanced modal FRF denominator function range. This is completely similar to the procedure for the MR strategy described in Section 3.2.2, and therefore is not repeated here. Since the MRE method clearly reduces the conservatism in the $\langle \hat{k}_i, \hat{m}_i \rangle$-domain approximation of every mode, it also reduces the conservatism in the total envelope FRF. This will be illustrated on the numerical examples in the second part of this paper.

4. Extension of the interval procedures to damped frequency-response function analysis

This section focusses on the FRF analysis of uncertain structures defined with interval uncertainties. It aims at the extension of the envelope FRF analysis described in the previous section to damped structures.

4.1. Introduction of damping in the interval FRF algorithm

Very often there is insufficient information to describe the damping properties of a structure exactly. Therefore, modelling the damping mechanisms numerically proves to be an extremely difficult task. This has given rise to a number of simplified damping models. These are inspired by

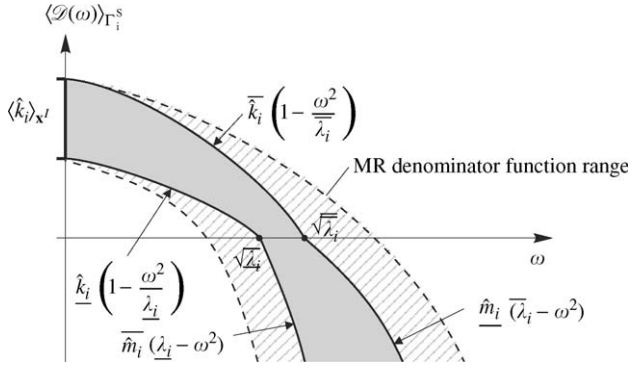

Fig. 8. Modal FRF denominator function range of a positive mode using the MRE method.

mathematical considerations rather than by physical representation of the damping phenomena. The fact that these simplified damping models are extremely popular does not mean that they are always equally successful. It is clear that they are subject to uncertainty. However, they have proven to adequately represent low damping while simultaneously, they simplify the computational procedures in the FE response analysis.

One of the most commonly applied damping models is Rayleigh (or proportional) damping. In this model, the damping matrix is assumed to be a linear combination of the system mass and stiffness matrices

$$\mathbf{C} = \alpha_K \mathbf{K} + \alpha_M \mathbf{M}. \tag{26}$$

This paper now focusses on the implications of proportional damping on the envelope FRF analysis. A damping model with constant values for α_K and α_M is assumed. The proportional coupling propagates the interval uncertainties on the stiffness and mass properties of the model to the damping properties. It is clear that any damping interval can be obtained through the choice of the proportional constants. However, since the damping in the analysis always varies proportionally with the stiffness and mass properties through a constant linear combination, the values inside this damping interval are not independently combined with all values in the mass and stiffness intervals. Therefore, using this approach, damping cannot be implemented as an independent source of uncertainty.

Applying the modal superposition procedure on proportionally damped structures, the total FRF equals

$$\mathrm{FRF}_{jk} = \sum_{i=1}^{n} \frac{1}{(\hat{k}_i - \omega^2 \hat{m}_i) + \jmath\,(\alpha_K \hat{k}_i + \alpha_M \hat{m}_i)\omega} \tag{27}$$

with $\hat{k}_i$ and $\hat{m}_i$ the normalised modal parameters as defined in Eqs. (5) and (6). Eq. (27) shows that the damped FRF calculation through the modal superposition principle is very similar to the undamped case. As for the undamped case, the modal FRF contributions depend on the model input parameters only through the modal stiffness and mass. This means that also for the proportionally damped case, the range of the modal contributions can be calculated if the range of the modal parameters is known. Both the MR and the MRE $\langle \hat{k}_i, \hat{m}_i \rangle$-domain approximations defined in the undamped procedure can be used for this purpose, since they define a conservative approximation of the area of possible $(\hat{k}_i, \hat{m}_i)$ combinations in the modal space with respect to the interval input parameter space. Consequently, in order to extend the undamped procedure to proportionally damped structures, the behaviour of the damped modal FRF over the bounded domain in the modal space has to be analysed.

Compared to the undamped case, the main difference is in the fact that the modal FRF contributions now are complex functions. The procedure handles this by treating the real and the complex parts of the response separately. For both parts, the response range is calculated for each mode. The superposition then constructs the range of the real and imaginary parts of the total response by adding together all real, respectively, imaginary modal FRF contributions. Finally, based on these results, the amplitude and phase are directly derived from the total real and imaginary envelope FRFs. The algorithm can be summarised as follows:

1. for all considered modes
   (a) calculate the $\langle \hat{k}_i, \hat{m}_i \rangle$-domain approximation (similar to the undamped case),

(b) calculate the range of the modal real and imaginary FRF based on the $\langle \hat{k}_i, \hat{m}_i \rangle$-domain approximation,

2. sum the modal real and imaginary envelope FRFs to obtain a conservative approximation of the total real and imaginary envelope FRFs,
3. post-process the real and imaginary parts to obtain the total amplitude and phase envelope FRF.

The first step on the modal level (step 1(a)) is completely similar to the undamped case and, therefore, not repeated here. The core of the development is in step 1(b) which consists of the analytical derivation of the modal real and imaginary envelope FRFs given the $\langle \hat{k}_i, \hat{m}_i \rangle$-domain approximation. Section 4.2 describes this in detail for, respectively, the real and imaginary part of a damped modal FRF contribution of a positive mode. The results are then extended to negative modes in Section 4.3. For the treatment of switch modes, the reader is referred to Ref. [17]. Finally, Section 4.4 describes the superposition of the modal contributions to a total real and imaginary envelope FRF, and how these should be further processed in order to obtain the amplitude and phase envelope FRF.

4.2. Damped modal FRF contributions

4.2.1. Real part analysis

The real part of the modal FRF in Eq. (27) equals

$$\Re(\mathrm{FRF}_{jk}^{i}) = \frac{\hat{k}_i - \omega^2 \hat{m}_i}{(\hat{k}_i - \omega^2 \hat{m}_i)^2 + (\alpha_K \hat{k}_i + \alpha_M \hat{m}_i)^2 \omega^2}. \tag{28}$$

This is further referred to as the modal real FRF, and can be regarded as a function of the two modal parameters $\hat{k}_i$ and $\hat{m}_i$. Fig. 9 illustrates a possible behaviour of this modal real FRF as a function of $\hat{k}_i$ and $\hat{m}_i$. The IFE procedure requires the calculation of the range of this function taking into account that the modal parameters are inside the used $\langle \hat{k}_i, \hat{m}_i \rangle$-domain approximation. It is now shown how this range can be derived analytically by analysing the surface that describes the evolution of the real part of the response above the $\langle \hat{k}_i, \hat{m}_i \rangle$-domain approximation. Fig. 9

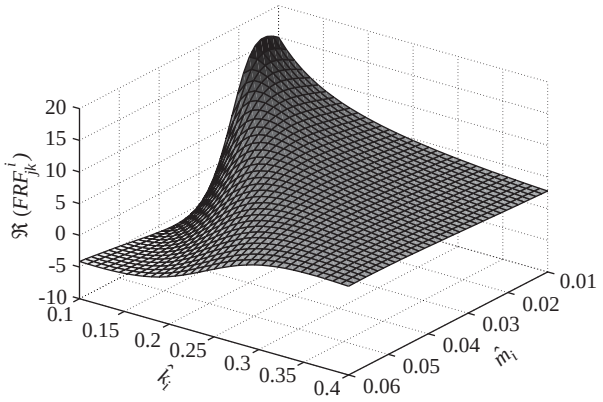

Fig. 9. Evolution of the modal real FRF in the modal parameter space.

illustrates this surface for a specific frequency. It is important to note that this surface varies with the frequency, which means that also the derived bounds should be expressed as frequency-dependent functions.

A first important observation concerns the evolution of the modal real FRF over radial lines in the modal parameter space. By substituting the modal parameters in Eq. (28) by equivalent radial coordinates using $\hat{k}_i = r\sin\theta$ and $\hat{m}_i = r\cos\theta$, the modal real FRF equals

$$\Re(\mathrm{FRF}^i_{jk}) = \frac{1}{r}\left(\frac{\sin\theta - \omega^2\cos\theta}{(\sin\theta - \omega^2\cos\theta)^2 + (\alpha_K\sin\theta + \alpha_M\cos\theta)^2\omega^2}\right). \tag{29}$$

For a constant angle θ, this is clearly a monotonic function of the radius r. Taking into account the geometrical form of the MR and MRE $\langle\hat{k}_i, \hat{m}_i\rangle$-domain approximations (see Figs. 3 and 7), this implies that for both strategies, the extrema of the modal real FRF are located either on the horizontal or on the vertical boundaries of the $\langle\hat{k}_i, \hat{m}_i\rangle$-domain approximation. However, it is impossible to predict on which of these four border lines the global extrema are located. Furthermore, this location of the modal response extrema on the border lines depends on the frequency. Therefore, each border line has to be investigated individually for the complete frequency domain. The global extrema then can be easily derived by comparing the envelope functions for each individual border line. The procedure to calculate the modal real FRF envelope can be summarised to the following steps:

1. the calculation of the lower and upper bounds on the real FRF considering modal parameter combinations on the individual vertical and horizontal border lines of the $\langle\hat{k}_i, \hat{m}_i\rangle$-domain approximation,
2. the calculation of the global lower and upper bounds on the modal real FRF by taking the maximum of all upper bounds and minimum of all lower bounds of the envelope functions resulting from the previous step.

The only difference between the MR and the MRE strategy is that through the introduction of the eigenvalue boundaries in the MRE $\langle\hat{k}_i, \hat{m}_i\rangle$-domain approximation, the section of the horizontal and vertical lines that has to be analysed in the first step is reduced in length. For both strategies, the core of the procedure is the analytical description of the modal real FRF above-bounded horizontal and vertical lines in the modal parameter space, based on which the range of the function can be derived. The remainder of this section describes an analytical method for this derivation for both vertical and horizontal lines, using arbitrary bounds on these lines. This method can be applied for both the MR and the MRE strategy by proper introduction of the geometrical properties of the $\langle\hat{k}_i, \hat{m}_i\rangle$-domain approximation into the procedure, i.e. the coordinates of the bounding points of the horizontal and vertical lines that need to be analysed. For the MR method, these are the coordinates of the corners of the modal rectangle. For the MRE method, these are the coordinates of the upper right and lower left MR corners completed with the coordinates of the corner points c_i from Fig. 7.

4.2.1.1. Vertical lines in the modal parameter space. For the analysis of a vertical line in the modal parameter space, a constant value m^* is introduced for the modal mass parameter in Eq. (28). This results in a function $\Re(\mathrm{FRF}^i_{jk})_{m^*}$ which has only $\hat{k}_i$ as variable. The analysis now

focusses on the variation of this function when the modal stiffness parameter varies over a positive interval $[\underline{k}, \overline{k}]$. It can be shown that the modal real FRF as a function of $\hat{k}_i$ has exactly one minimum and one maximum as illustrated in Fig. 10. The extrema are reached for $\hat{k}_i$ equal to, respectively,

$$k_+(\omega) = m^* \left(\omega^2 + \frac{\omega(\alpha_K \omega^2 + \alpha_M)}{\sqrt{1 + \alpha_K^2 \omega^2}} \right), \tag{30}$$

$$k_-(\omega) = m^* \left(\omega^2 - \frac{\omega(\alpha_K \omega^2 + \alpha_M)}{\sqrt{1 + \alpha_K^2 \omega^2}} \right). \tag{31}$$

The explicit function of ω indicates that the locations of the extrema depend on the frequency. This is important for the derivation of the modal real FRF bounds. To analyse the evolution of these bounds, $k_-(\omega)$ and $k_+(\omega)$ are analysed in the frequency domain. Fig. 11 illustrates the global form of both functions. The location of the maximum $k_+(\omega)$ is a monotonically increasing function over the frequency domain. The location of the minimum $k_-(\omega)$ has a horizontal asymptote at $\hat{k}_i = k_-^{\infty}$. Both functions start in the origin of the $\hat{k}_i$-axis in Fig. 11. This means that for low frequencies, both extrema in Fig. 10 are located to the left-hand side of any positive $[\underline{k}, \overline{k}]$ interval on the $\hat{k}_i$-axis. For increasing frequency, both extrema approach and possibly cross the interval. This can be interpreted as if the response function of Fig. 10 evolves globally to the right relative to the $[\underline{k}, \overline{k}]$ interval. The implications of this evolution for the lower and upper bound of the response is discussed by analysing the frequency domain in increasing direction.

- *The lower response bound*: For small frequencies, both extrema are situated to the left of the $[\underline{k}, \overline{k}]$ interval. Therefore, the lower bound on the real response corresponds to the upper bound of the interval as indicated in Fig. 12(a). When the frequency increases, the response function shifts to the right and the response maximum enters the $[\underline{k}, \overline{k}]$ interval. Further, a frequency is reached for which the response values are equal for $\underline{k}$ and $\overline{k}$ (Fig. 12(b)). From this frequency

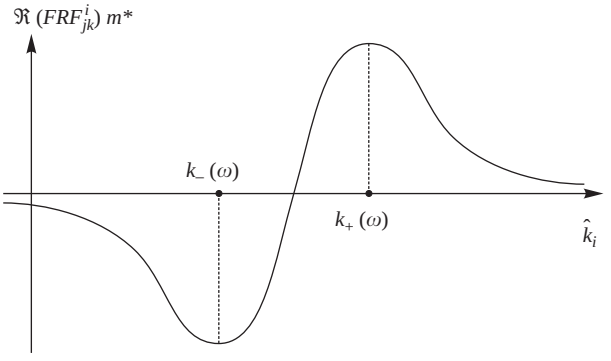

Fig. 10. Evolution of the modal real FRF over the $\hat{k}_i$ domain for a constant modal mass value.

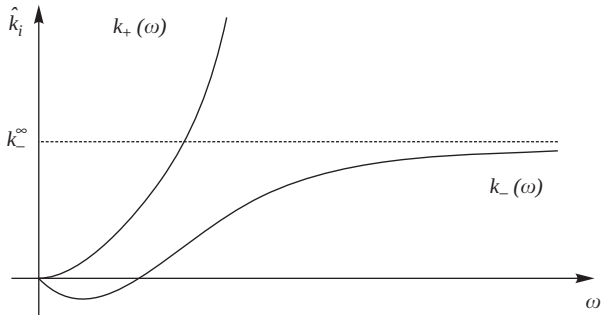

Fig. 11. Evolution of $k_-(\omega)$ and $k_+(\omega)$ in the frequency domain.

on, the response minimum is located on the lower bound of the $[\underline{k}, \overline{k}]$ interval (Fig. 12(c)). When the frequency increases further, the response minimum enters the $[\underline{k}, \overline{k}]$ interval for some frequency if the asymptotic value k_-^∞ lies above $\underline{k}$. Starting from this frequency, the response minimum is located in the extremum inside the $[\underline{k}, \overline{k}]$ interval (Fig.12(d)) and the minimal value of the response is obtained for the corresponding $k_-(\omega)$ values. Finally, if the asymptotic value k_-^∞ lies above the $[\underline{k}, \overline{k}]$ interval, the response minimum reaches the upper bound of the interval for some frequency. From this frequency on, the function over the interval becomes monotonically decreasing and the response minimum is located in the upper bound of the interval (Fig. 12(e)).

- *The upper response bound*: For small frequencies, both extrema are situated to the left of the $[\underline{k}, \overline{k}]$ interval. Therefore, the upper bound on the response corresponds to the lower bound of the interval as indicated in Fig. 12(a). Since $k_+(\omega)$ is monotonically increasing, the location of the response maximum always for some frequency enters the $[\underline{k}, \overline{k}]$ interval. Starting from this frequency, the response maximum is located in the extremum inside the $[\underline{k}, \overline{k}]$ interval (Fig. 12(b)). For these frequencies, the maximal value of the response is obtained for the corresponding $k_+(\omega)$ values. Once the response maximum has reached the upper bound of the $[\underline{k}, \overline{k}]$ interval, the response maximum is located in the upper bound of the interval (Fig. 12(c)). When the frequency increases further, the response minimum enters the $[\underline{k}, \overline{k}]$ interval if the asymptotic value k_-^∞ lies above $\underline{k}$. It can be proven that if the asymptotic value lies above the midpoint of the $[\underline{k}, \overline{k}]$ interval, a frequency is reached for which the response values are equal for $\underline{k}$ and $\overline{k}$ (Fig. 12(d)). From this frequency on, the response maximum is located on the lower bound of the $[\underline{k}, \overline{k}]$ interval (Fig. 12(e)).

This description shows that the exact upper and lower bounds on the modal real FRF above an interval on a vertical line in the modal parameter space follow directly from an analytical procedure. The procedure consists of selecting the correct $\hat{k}_i$ value which, combined with the m^* value at the vertical line, yields the bounds of the modal real FRF. This correct $\hat{k}_i$ value always lies either on one of the bounds of the $[\underline{k}, \overline{k}]$ interval, either in an extremum of the modal real FRF inside the interval. The evolution of this $\hat{k}_i$ value as a function of ω corresponding to the descriptions above is illustrated in Fig. 13(a) for the lower bound and in Fig. 13(b) for the upper bound.

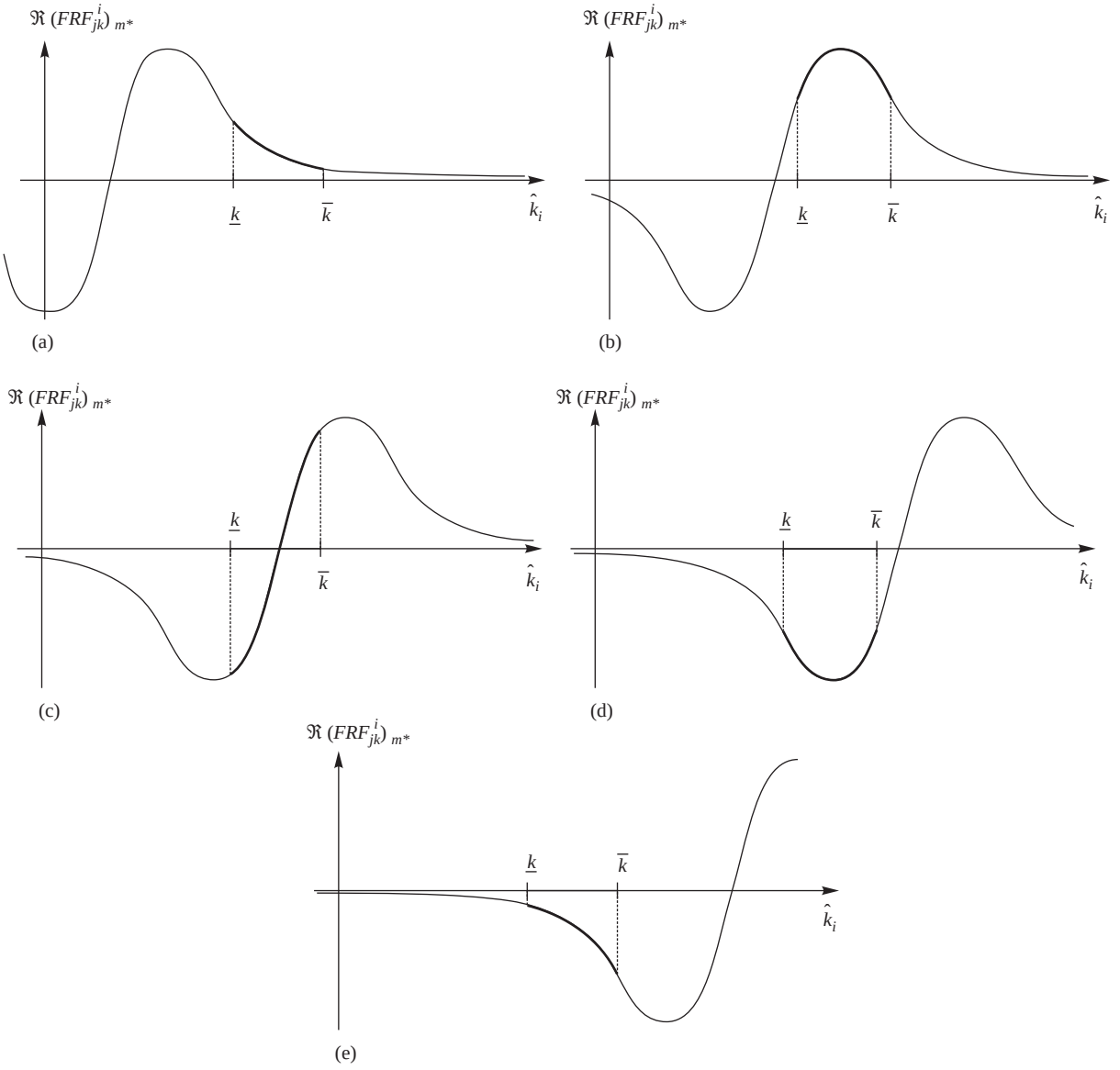

Fig. 12. (a)–(e) Evolution of the modal real FRF above an interval on a vertical line in the modal parameter space for increasing frequencies.

The frequencies ω_1^l, ω_2^l, ω_1^u and ω_2^u represent the points where, respectively, $k_-(\omega)$ and $k_+(\omega)$ cross with $\hat{k}_i = \underline{k}$ and $\hat{k}_i = \overline{k}$. Therefore, they satisfy

$$\underline{k} = m^* \left({\omega_1^l}^2 - \frac{\omega_1^l(\alpha_K {\omega_1^l}^2 + \alpha_M)}{\sqrt{1 + \alpha_K^2 {\omega_1^l}^2}} \right), \tag{32}$$

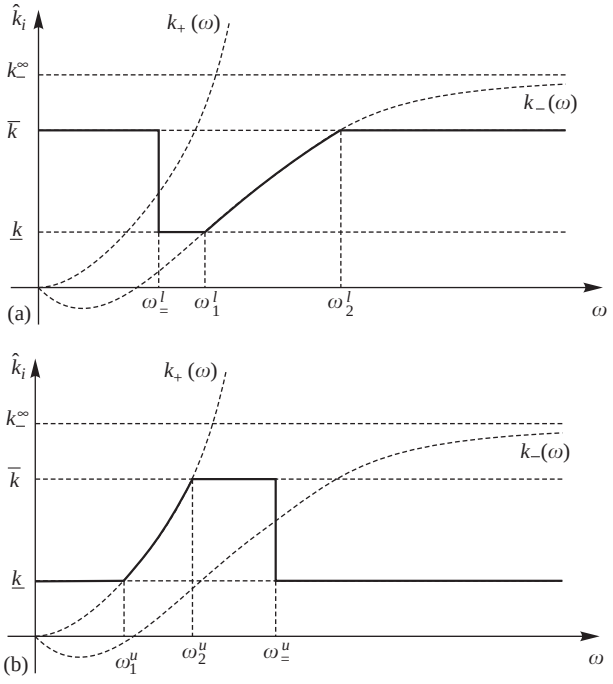

Fig. 13. Evolution of the $\hat{k}_i$ value corresponding to the extrema of the modal real FRF at a vertical line in the modal parameter space: (a) lower bound and (b) upper bound.

$$\overline{k} = m^* \left({\omega_2^l}^2 - \frac{\omega_2^l(\alpha_K {\omega_2^l}^2 + \alpha_M)}{\sqrt{1 + \alpha_K^2 {\omega_2^l}^2}} \right), \tag{33}$$

$$\underline{k} = m^* \left(\omega_1^{u2} + \frac{\omega_1^u(\alpha_K \omega_1^{u2} + \alpha_M)}{\sqrt{1 + \alpha_K^2 \omega_1^{u2}}} \right), \tag{34}$$

$$\overline{k} = m^* \left(\omega_2^{u2} + \frac{\omega_2^u(\alpha_K \omega_2^{u2} + \alpha_M)}{\sqrt{1 + \alpha_K^2 \omega_2^{u2}}} \right). \tag{35}$$

Furthermore, $\omega_=^l$ and $\omega_=^u$ follow directly from satisfying the equation:

$$\Re(\mathrm{FRF}_{jk}^i(\omega_=))_{\underline{k},m^*} = \Re(\mathrm{FRF}_{jk}^i(\omega_=))_{\overline{k},m^*}. \tag{36}$$

This means that the curve of optimal $\hat{k}_i$ values given in Fig. 13 is completely described analytically, and the bounds on the real FRF over the vertical line can be calculated by substituting the values on this curve into Eq. (28).

4.2.1.2. Horizontal lines in the modal parameter space. The procedure to calculate the bounds on the modal real FRF above a horizontal line in the modal parameter space is very similar to the one for the vertical lines described above. A constant value k^* is introduced for the modal stiffness parameter in Eq. (28). This results in a function $\Re(\mathrm{FRF}^i_{jk})_{k^*}$ which has only $\hat{m}_i$ as variable. The analysis now focusses on the variation of this function when the modal mass parameter varies over a positive interval $[\underline{m},\overline{m}]$. It can be shown that the resulting function of $\hat{m}_i$ has exactly one maximum and one minimum as illustrated in Fig. 14. The extrema are reached for $\hat{m}_i$ equal to, respectively,

$$m_+(\omega) = k^* \left(\frac{1}{\omega^2} + \frac{\alpha_M + \alpha_K \omega^2}{\omega^2 \sqrt{\omega^2 + \alpha_M^2}} \right) \tag{37}$$

$$m_-(\omega) = k^* \left(\frac{1}{\omega^2} - \frac{\alpha_M + \alpha_K \omega^2}{\omega^2 \sqrt{\omega^2 + \alpha_M^2}} \right) \tag{38}$$

To analyse the evolution of the bounds of the modal real FRF for all frequencies, $m_-(\omega)$ and $m_+(\omega)$ are analysed analytically in the frequency domain. Fig. 15 illustrates the global form of both functions. The location of the minimum $m_+(\omega)$ is a monotonically decreasing function over the frequency domain. The location of the maximum $m_-(\omega)$ starts from m^0_- on the $\hat{m}_i$-axis. Both $m_+(\omega)$ and $m_-(\omega)$ tend to zero when ω tends to infinity.

The implications of the evolution of $m_-(\omega)$ and $m_+(\omega)$ for the lower and upper bound of the response is similar to the description for the vertical boundary in Fig. 12. The difference is that in this case the locations of the extrema decrease for increasing ω and that the minimum and maximum have switched positions. Still, the exact upper and lower bounds on the modal real FRF above an interval on a horizontal line in the modal parameter space follow directly from a similar analytical procedure. The procedure consists of selecting the correct $\hat{m}_i$ value which, combined with the k^* value at the horizontal line, yields the lower and upper bound of the modal real FRF. The evolution of this correct $\hat{m}_i$ value as a function of ω is illustrated in Fig. 16(a) for the lower bound and in Fig. 16(b) for the upper bound.

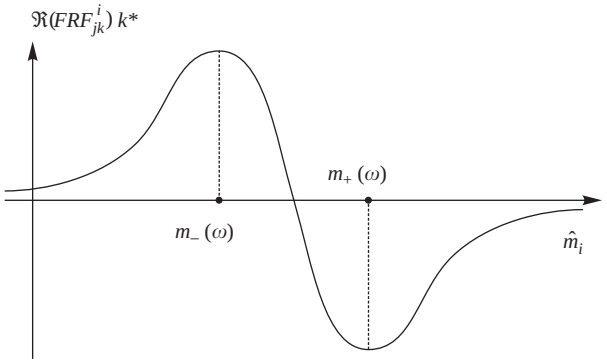

Fig. 14. Evolution of the modal real FRF over the $\hat{m}_i$ domain for a constant modal stiffness value.

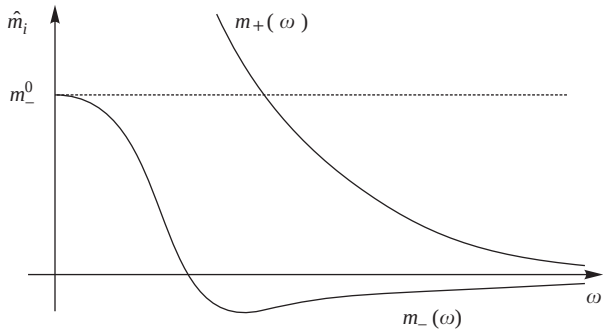

Fig. 15. Evolution of $m_-(\omega)$ and $m_+(\omega)$ in the frequency domain.

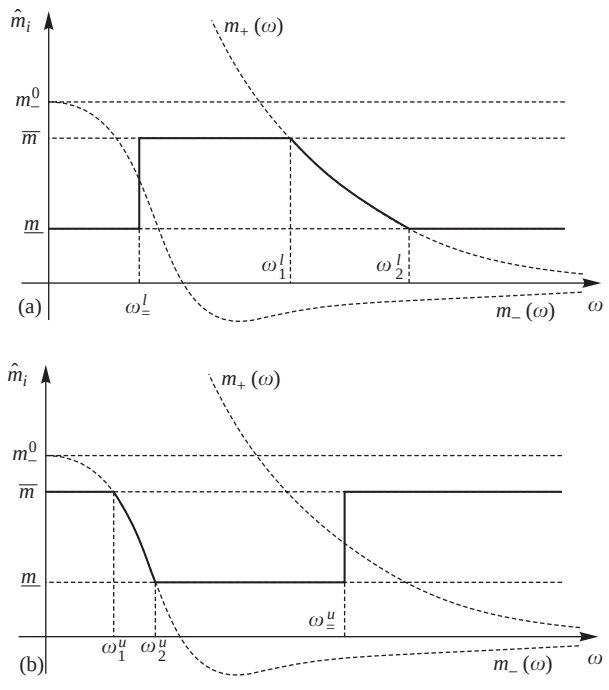

Fig. 16. Evolution of the $\hat{m}_i$ value corresponding to the extrema of the modal real FRF at a horizontal line in the modal parameter space: (a) lower bound and (b) upper bound.

The frequencies ω_1^l, ω_2^l, ω_1^u and ω_2^u represent the points where, respectively, $m_+(\omega)$ and $m_-(\omega)$ cross with $\hat{m}_i = \overline{m}$ and $\hat{m}_i = \underline{m}$. Therefore, they satisfy

$$\overline{m} = k^* \left(\frac{1}{{\omega_1^l}^2} + \frac{\alpha_M + \alpha_K {\omega_1^l}^2}{{\omega_1^l}^2 \sqrt{{\omega_1^l}^2 + \alpha_M^2}} \right), \tag{39}$$

$$\underline{m} = k^* \left(\frac{1}{\omega_2^{l\,2}} + \frac{\alpha_M + \alpha_K \omega_2^{l\,2}}{\omega_2^{l\,2} \sqrt{\omega_2^{l\,2} + \alpha_M^2}} \right), \tag{40}$$

$$\overline{m} = k^* \left(\frac{1}{\omega_1^{u2}} - \frac{\alpha_M + \alpha_K \omega_1^{u2}}{\omega_1^{u2} \sqrt{\omega_1^{u2} + \alpha_M^2}} \right), \tag{41}$$

$$\underline{m} = k^* \left(\frac{1}{\omega_2^{u2}} - \frac{\alpha_M + \alpha_K \omega_2^{u2}}{\omega_2^{u2} \sqrt{\omega_2^{u2} + \alpha_M^2}} \right). \tag{42}$$

Furthermore, $\omega_=^l$ and $\omega_=^u$ follow directly from satisfying the equation:

$$\Re(\mathrm{FRF}_{jk}^i(\omega_=))_{\underline{m},k^*} = \Re(\mathrm{FRF}_{jk}^i(\omega_=))_{\overline{m},k^*}. \tag{43}$$

This means that the curve of optimal $\hat{m}_i$ values given in Fig. 16 is completely described analytically, and the bounds on the real FRF over the horizontal line can be calculated by substituting the values on this curve into Eq. (28).

4.2.2. Imaginary part analysis

The imaginary part of the modal FRF in Eq. (27) equals

$$\Im(\mathrm{FRF}_{jk}^i) = \frac{-\omega(\alpha_K \hat{k}_i + \alpha_M \hat{m}_i)}{(\hat{k}_i - \omega^2 \hat{m}_i)^2 + (\alpha_K \hat{k}_i + \alpha_M \hat{m}_i)^2 \omega^2}. \tag{44}$$

This is further referred to as the modal imaginary FRF. Again, the IFE procedure requires the calculation of the range of this function taking into account that the modal parameters are inside the $\langle \hat{k}_i, \hat{m}_i \rangle$-domain approximation.

As for the real part, a radial analysis is performed by substituting the modal parameters in Eq. (44) by equivalent radial coordinates $\hat{k}_i = r \sin\theta$ and $\hat{m}_i = r \cos\theta$

$$\Im(\mathrm{FRF}_{jk}^i) = -\frac{1}{r} \left(\frac{\omega(\alpha_K \sin\theta + \alpha_M \cos\theta)}{(\sin\theta - \omega^2 \cos\theta)^2 + (\alpha_K \sin\theta + \alpha_M \cos\theta)^2 \omega^2} \right). \tag{45}$$

Also here, for a constant angle θ, this is clearly a monotonic function of the radius r. Again, this implies that for both the MR and MRE strategy, the extrema of the modal imaginary FRF are located either on the horizontal or on the vertical boundaries of the $\langle \hat{k}_i, \hat{m}_i \rangle$-domain approximation. Completely similar to the real part analysis, the procedure to calculate the resulting modal imaginary envelope FRF relies completely on the derivation of the modal imaginary FRF range over horizontal and vertical bounded lines in the modal space.

4.2.2.1. Vertical lines in the modal parameter space. The introduction of a constant value m^* for the modal mass parameter in Eq. (44) results in a function $\Im(\mathrm{FRF}_{jk}^i)_{m^*}$ which has only $\hat{k}_i$ as variable. The analysis now focusses on the variation of this function when $\hat{k}_i$ varies over a positive interval $[\underline{k}, \overline{k}]$. It can be shown that the modal imaginary FRF as a function of $\hat{k}_i$ has exactly one

maximum and one minimum as illustrated in Fig. 17. The extrema are reached for $\hat{k}_i$ equal to, respectively,

$$k_+(\omega) = m^* \left(-\frac{\alpha_M}{\alpha_K} + \frac{\alpha_K \omega^2 + \alpha_M}{\alpha_K \sqrt{1 + \alpha_K^2 \omega^2}} \right), \tag{46}$$

$$k_-(\omega) = m^* \left(-\frac{\alpha_M}{\alpha_K} - \frac{\alpha_K \omega^2 + \alpha_M}{\alpha_K \sqrt{1 + \alpha_K^2 \omega^2}} \right). \tag{47}$$

It is easily shown that $k_-(\omega)$ is negative for all frequencies. Therefore, it is of no importance in the derivation of the response bounds over a positive $[\underline{k}, \overline{k}]$ interval. The location of the minimum $k_+(\omega)$ has possibly a local minimum, after which it asymptotically tends to infinity as illustrated in Fig. 18.

The exact upper and lower bounds on the modal imaginary FRF above an interval on a vertical line in the modal parameter space follow directly from an analytical procedure similar to the modal real FRF range calculation. The procedure is simpler because the response now only has one extremum that has to be taken into account. The procedure consists of selecting the correct $\hat{k}_i$ value which, combined with the m^* value at the vertical line yields the lower and upper bound of the modal imaginary FRF. The evolution of this optimal $\hat{k}_i$ value as a function of ω is illustrated in Fig. 19(a) for the lower bound and in Fig. 19(b) for the upper bound.

The frequencies ω_1^l and ω_2^l represent the points where $k_+(\omega)$ crosses, respectively, with $\hat{k}_i = \underline{k}$ and $\hat{k}_i = \overline{k}$. Therefore, they satisfy

$$\underline{k} = m^* \left(-\frac{\alpha_M}{\alpha_K} + \frac{\alpha_K {\omega_1^l}^2 + \alpha_M}{\alpha_K \sqrt{1 + \alpha_K^2 {\omega_1^l}^2}} \right), \tag{48}$$

$$\overline{k} = m^* \left(-\frac{\alpha_M}{\alpha_K} + \frac{\alpha_K {\omega_2^l}^2 + \alpha_M}{\alpha_K \sqrt{1 + \alpha_K^2 {\omega_2^l}^2}} \right). \tag{49}$$

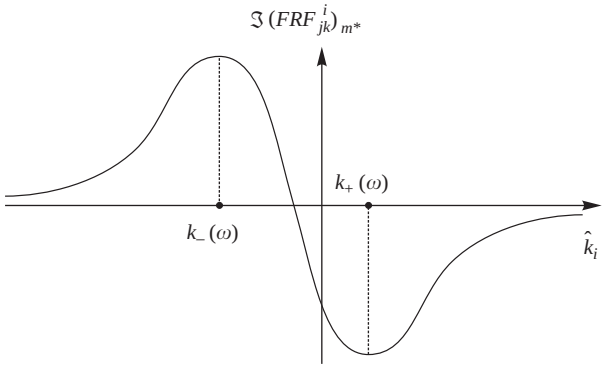

Fig. 17. Evolution of the modal imaginary FRF over the $\hat{k}_i$ domain for a constant modal mass value.

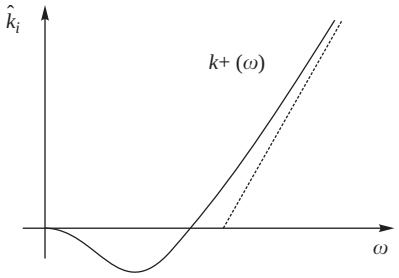

Fig. 18. Evolution of $k_+(\omega)$ in the frequency domain.

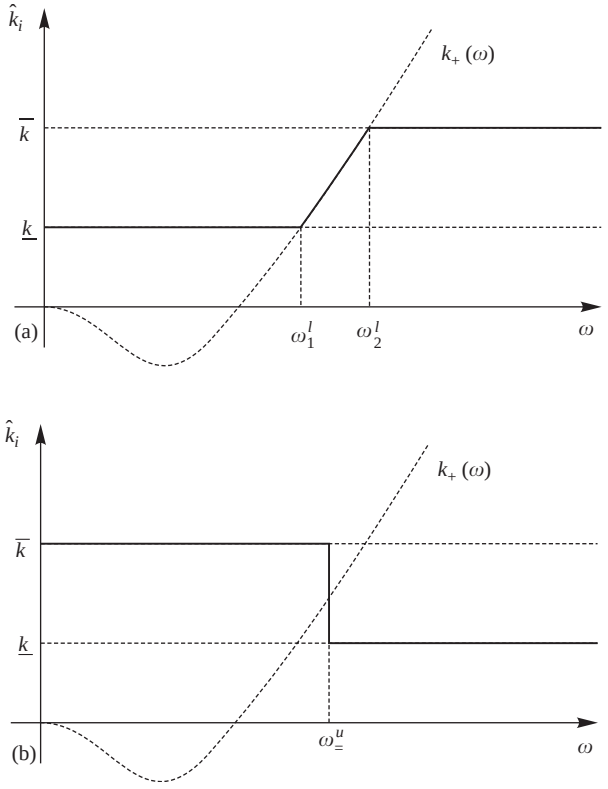

Fig. 19. Evolution of the $\hat{k}_i$ value corresponding to the extrema of the modal imaginary FRF at a vertical line in the modal parameter space: (a) lower bound and (b) upper bound.

Furthermore, $\omega_=^u$ follows directly from satisfying the equation:

$$\Im(\mathrm{FRF}_{jk}^i(\omega_=^u))_{\underline{k},m^*} = \Im(\mathrm{FRF}_{jk}^i(\omega_=^u))_{\overline{k},m^*}. \tag{50}$$

This means that the curve of optimal $\hat{k}_i$ values given in Fig. 19 is completely described analytically, and the bounds on the imaginary FRF over the vertical line can be calculated by substituting the values on this curve into Eq. (44).

4.2.2.2. Horizontal lines in the modal parameter space. The introduction of a constant value k^* for the modal stiffness parameter in Eq. (44) results in a function $\Im(\mathrm{FRF}^i_{jk})_{k^*}$ which has only $\hat{m}_i$ as variable. The analysis focusses on the variation of this function when $\hat{m}_i$ varies over a positive interval $[\underline{m}, \overline{m}]$. It can be shown that the modal imaginary FRF as a function of $\hat{m}_i$ has exactly one maximum and one minimum as illustrated in Fig. 20. The extrema are reached for $\hat{m}_i$ equal to, respectively,

$$m_+(\omega) = k^* \left(-\frac{\alpha_K}{\alpha_M} + \frac{\alpha_K \omega^2 + \alpha_M}{\alpha_M \omega \sqrt{\alpha_M^2 + \omega^2}} \right), \tag{51}$$

$$m_-(\omega) = k^* \left(-\frac{\alpha_K}{\alpha_M} - \frac{\alpha_K \omega^2 + \alpha_M}{\alpha_M \omega \sqrt{\alpha_M^2 + \omega^2}} \right). \tag{52}$$

It is easily shown that $m_-(\omega)$ is negative for all frequencies. Therefore, it is not of importance in the derivation of the response bounds over a positive $[\underline{m}, \overline{m}]$ interval. The location of the minimum $m_+(\omega)$ starts from infinity at $\omega = 0$ after which it possibly has a local minimum. Finally, it tends to zero when the frequency tends to infinity. Fig. 21 illustrates its global form.

The exact upper and lower bounds on the modal imaginary FRF above an interval on a horizontal line in the modal parameter space follow directly from an analytical procedure similar to the procedure for a vertical line. The procedure consists of selecting the correct $\hat{m}_i$ value which, combined with the k^* value at the horizontal line yields the lower and upper bound of the modal imaginary FRF. Again, the optimal $\hat{m}_i$ value always lies either on one of the bounds of the $[\underline{m}, \overline{m}]$ interval, either in the extremum of the modal imaginary FRF inside the interval. The evolution of this optimal $\hat{m}_i$ value as a function of ω is illustrated in Fig. 22(a) for the lower bound and in Fig. 22(b) for the upper bound.

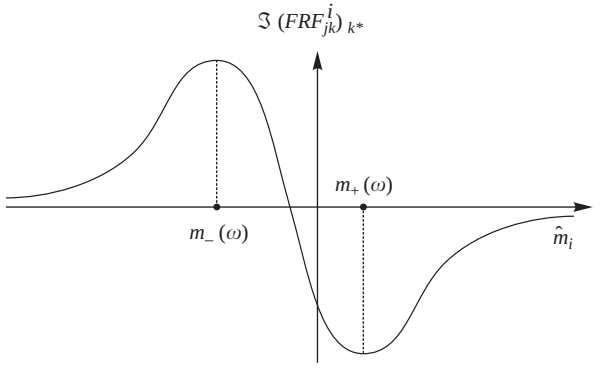

Fig. 20. Evolution of the modal imaginary FRF over the $\hat{m}_i$ domain for a constant modal stiffness value.

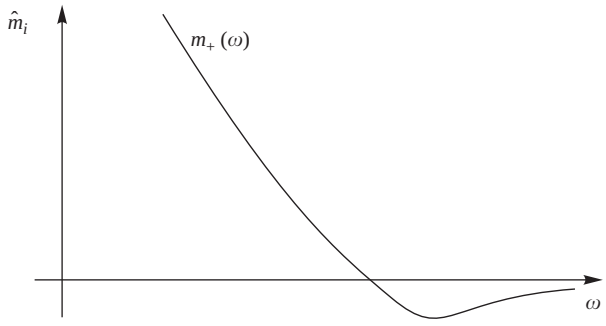

Fig. 21. Evolution of $m_+(\omega)$ in the frequency domain.

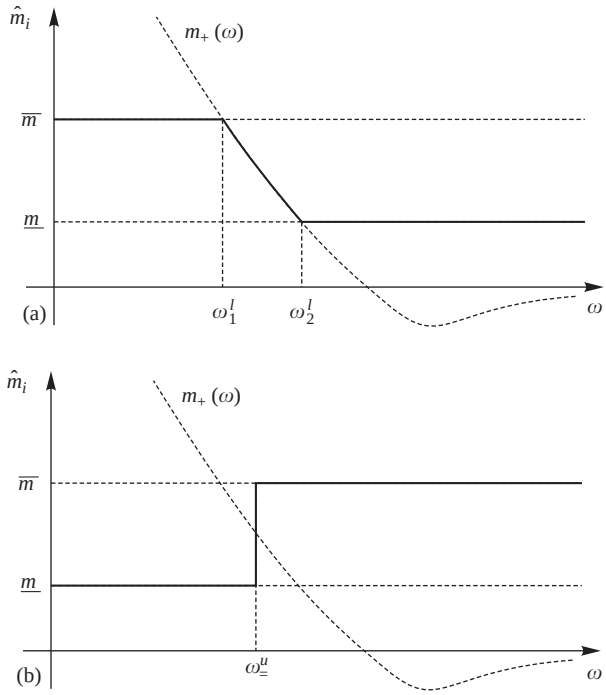

Fig. 22. Evolution of the $\hat{m}_i$ value corresponding to the extrema of the modal imaginary FRF at a horizontal line in the modal parameter space: (a) lower bound and (b) upper bound.

The frequencies ω_1^l and ω_2^l represent the points where $m_+(\omega)$ crosses, respectively, with $\hat{m}_i = \overline{m}$ and $\hat{m}_i = \underline{m}$. Therefore, they satisfy

$$\overline{m} = k^* \left(-\frac{\alpha_K}{\alpha_M} + \frac{\alpha_K \omega_1^{l\,2} + \alpha_M}{\alpha_M \omega \sqrt{\alpha_M^2 + \omega_1^{l\,2}}} \right), \tag{53}$$

$$\underline{m} = k^* \left(-\frac{\alpha_K}{\alpha_M} + \frac{\alpha_K \omega_2^{l\,2} + \alpha_M}{\alpha_M \omega \sqrt{\alpha_M^2 + \omega_2^{l\,2}}} \right). \tag{54}$$

Furthermore, $\omega_{=}^{u}$ follows directly from satisfying the equation:

$$\Im(\mathrm{FRF}_{jk}^{i}(\omega_{=}^{u}))_{\underline{m},k^*} = \Im(\mathrm{FRF}_{jk}^{i}(\omega_{=}^{u}))_{\overline{m},k^*} \tag{55}$$

This means that the curve of optimal $\hat{m}_i$ values given in Fig. 22 is completely described analytically, and the bounds on the imaginary FRF over the horizontal line can be calculated by substituting the values on this curve into Eq. (44).

4.3. The modal envelope FRF for negative modes

The analytical procedures in Sections 4.2.1 and 4.2.2 consider only positive ranges for the modal parameters. They require that the $\langle \hat{k}_i, \hat{m}_i \rangle$-domain approximations of the analysed modes are located in the first quadrant of the modal parameter space, and, therefore, are limited to positive modes. The goal is to apply these procedures also for negative modes. This can be achieved by considering the MRE $\langle \hat{k}_i, \hat{m}_i \rangle$-domain approximation of a negative mode mirrored into the first quadrant of the modal parameter space. This is equivalent with switching the sign of the modal parameters. The corresponding horizontal and vertical boundaries on the mirrored modal parameters are then

$$\overline{-\hat{k}_i} = -(\underline{\hat{k}_i}), \tag{56}$$

$$\underline{-\hat{k}_i} = -(\overline{\hat{k}_i}), \tag{57}$$

$$\overline{-\hat{m}_i} = -(\underline{\hat{m}_i}), \tag{58}$$

$$\underline{-\hat{m}_i} = -(\overline{\hat{m}_i}). \tag{59}$$

The bounds on the eigenfrequency remain unchanged. The parameters $-\hat{k}_i$ and $-\hat{m}_i$ now are located in the first quadrant and, therefore, the procedures described in Sections 4.2.1 and 4.2.2 yield the bounds on $\Re(\mathrm{FRF}_{jk}^{i})_{-\hat{k}_i,-\hat{m}_i}$ and $\Im(\mathrm{FRF}_{jk}^{i})_{-\hat{k}_i,-\hat{m}_i}$. These now lead to the required boundary functions $\Re(\mathrm{FRF}_{jk}^{i})_{\hat{k}_i,\hat{m}_i}$ and $\Im(\mathrm{FRF}_{jk}^{i})_{\hat{k}_i,\hat{m}_i}$ using the following equality:

$$\Re(\mathrm{FRF}_{jk}^{i})_{\hat{k}_i,\hat{m}_i} = -\Re(\mathrm{FRF}_{jk}^{i})_{-\hat{k}_i,-\hat{m}_i}, \tag{60}$$

$$\Im(\mathrm{FRF}_{jk}^{i})_{\hat{k}_i,\hat{m}_i} = -\Im(\mathrm{FRF}_{jk}^{i})_{-\hat{k}_i,-\hat{m}_i}. \tag{61}$$

Eqs. (60) and (61) imply that the correct result of the procedure is achieved by compensating for the modal parameter sign inversion in the following way:

$$\underline{\Re(\mathrm{FRF}_{jk}^{i})_{\hat{k}_i,\hat{m}_i}} = -(\overline{\Re(\mathrm{FRF}_{jk}^{i})_{-\hat{k}_i,-\hat{m}_i}}), \tag{62}$$

$$\overline{\Re(\mathrm{FRF}_{jk}^{i})_{\hat{k}_i,\hat{m}_i}} = -(\underline{\Re(\mathrm{FRF}_{jk}^{i})_{-\hat{k}_i,-\hat{m}_i}}) \tag{63}$$

for the real part, and

$$\underline{\Im(\mathrm{FRF}^i_{jk})_{\hat{k}_i,\hat{m}_i}} = -(\overline{\Im(\mathrm{FRF}^i_{jk})_{-\hat{k}_i,-\hat{m}_i}}), \tag{64}$$

$$\overline{\Im(\mathrm{FRF}^i_{jk})_{\hat{k}_i,\hat{m}_i}} = -(\underline{\Im(\mathrm{FRF}^i_{jk})_{-\hat{k}_i,-\hat{m}_i}}) \tag{65}$$

for the imaginary part. The conclusion is that with an appropriate pre- and post-processing of the data used in and obtained from the procedures for the positive modes, the equivalent procedure for the negative modes is easily implemented.

4.4. Total amplitude and phase envelope FRF calculation

The total amplitude and phase envelope FRF are calculated using the total real and imaginary envelope FRFs. These result from the summation of the modal contributions derived in the previous section

$$\Re\mathrm{FRF}_{jk})^I = \sum_{i=1}^{n} \Re(\mathrm{FRF}^i_{jk})^I_{\cdot}, \tag{66}$$

$$\Im(\mathrm{FRF}_{jk})^I = \sum_{i=1}^{n} \Im(\mathrm{FRF}^i_{jk})^I_{\cdot} \tag{67}$$

This summation is easily implemented because the modal response contributions all describe a finite interval both for the real and the imaginary part of the FRF. Consequently, the summation of all lower, respectively, upper bounds yields the bounds on the total FRF.

The result of the summation is an interval range for the real and imaginary part of the complex response for every frequency. This means that it defines a rectangle in the complex space in which the response vector is contained. Based on this rectangle, an approximation of the amplitude range of the complex response is easily obtained by taking the points on the rectangle which are, respectively, the nearest and most distant from the origin. The phase range is derived in a similar

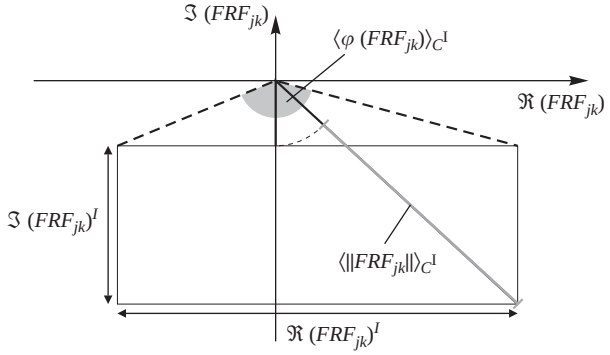

Fig. 23. Conversion of the real and imaginary FRF range to the amplitude and phase FRF range.

way. Fig. 23 illustrates this procedure. This results in

$$\langle \|\mathrm{FRF}_{jk}\| \rangle_{\mathscr{C}^I}, \tag{68}$$

$$\langle \varphi(\mathrm{FRF}_{jk}) \rangle_{\mathscr{C}^I} \tag{69}$$

with

$$\mathscr{C}^I = \left\{ \begin{array}{c} \Re(\mathrm{FRF}_{jk})^I \\ \Im(\mathrm{FRF}_{jk})^I \end{array} \right\}. \tag{70}$$

It should be noted that this final conversion to amplitude and phase envelope FRFs as shown in Fig. 23 considers the imaginary and real part of the FRF independently. Although the situation in the figure is exaggerated in order to clarify this point, this introduces an additional source of conservatism. This source is due to the fact that not every combination of real and imaginary parts within the rectangle is feasible. This is equivalent to the decoupling of the modal mass and stiffness in the modal space as discussed for the MR method. However, while in the modal domain the conservatism was introduced in the analysis of each individual mode, in the amplitude and phase conversion, the conservatism is introduced only through a single operation on the final response. Therefore, the introduced conservatism is limited, as will be shown in the numerical test cases in part two of this paper.

5. Conclusions

This paper describes a numerical procedure for numerical FRF analysis of damped structures with fuzzy uncertainties. It focusses on the numerical core of the analysis, i.e. the envelope FRF calculation. Because of the damping, the FRF is a complex function of the frequency. Generally, most interest is paid to the amplitude and phase of this complex function. Therefore, the goal of the procedure is to acquire the amplitude and phase envelope FRFs.

The development of the procedure starts from the MR and MRE methodology already available for undamped envelope FRF analysis. Using the proportional damping concept, the modal superposition principle remains the basis for the damped procedure. In the first step of the procedure, the real and imaginary parts of the modal envelope FRFs are calculated based on the MR or MRE approximations of the range of the modal parameters. In the next step, these real and imaginary modal contributions are summed to obtain the corresponding total envelope FRFs. The amplitude and phase envelope FRFs finally can be derived from the combination of the total real and imaginary envelope FRFs.

The calculation of the modal envelope FRFs proves to be the most challenging part of the numerical algorithm. This paper shows that, given the MR or MRE $\langle \hat{k}_i, \hat{m}_i \rangle$-domain approximation from the undamped procedure, it is always possible to obtain the exact bounds on the range of the real and imaginary part of the modal FRF analytically. These bounds always correspond to a combination of the modal parameters located in a point either on the horizontal or on the vertical border lines of the $\langle \hat{k}_i, \hat{m}_i \rangle$-domain approximation. Analytical procedures are derived to locate these combinations based on the geometrical description of the MR or MRE

$\langle \hat{k}_i, \hat{m}_i \rangle$-domain approximation. This finally results in an analytical procedure to derive the modal real and imaginary envelope FRFs.

Since all modal envelope FRFs obtained from the previous step consist of finite intervals, the summation to the total real and imaginary envelope FRF is straightforward. The calculation of the amplitude and phase range then combines independently the real and imaginary part of the total FRF. This yields a rectangular range in the complex space, from which the corresponding lower and upper bounds on the amplitude and phase are easily derived.

From a numerical point of view, the most relevant conclusion is that, using the principle of proportional damping, the total damped procedure proves to be an analytical extension of the undamped procedure. This means that the damped analysis does not require additional optimisation steps in the modal space. Therefore, the computation time for damped envelope FRFs is comparable to the computation time for the undamped envelope FRFs.

Acknowledgements

This research was funded by a post-doctoral fellowship from the Institute for the promotion of Innovation by Science and Technology in Flanders (IWT - Vlaanderen), Brussel.

References

[1] I. Elishakoff, Y. Ren, The bird's eye view on finite element method for structures with large stochastic variations, *Computer Methods in Applied Mechanics and Engineering* 168 (1999) 51–61.

[2] A. Haldar, S. Mahadevan, *Reliability Assessment Using Stochastic Finite Element Analysis*, Wiley, New York, 2000.

[3] W. Oberkampf, J. Helton, K. Sentz, Mathematical representation of uncertainty, in: *Non-Deterministic Approaches Forum*, *AIAA 2001-1645*, 2001.

[4] R. Rubenstein, *Simulation and the Monte Carlo Method*, Wiley, New York, 1981.

[5] D. Moens, D. Vandepitte, A survey of non-probabilistic uncertainty treatment in finite element analysis, *Computer Methods in Applied Mechanics and Engineering* 194 (14–16) (2005) 1527–1555.

[6] I. Elishakoff, D. Duan, Application of mathematical theory of interval analysis to uncertain vibrations, in: *Proceedings of the 1994 National Conference on Noise Control Engineering*, 1994, pp. 519–524.

[7] S. Chen, Z. Qiu, D. Song, A new method for computing the upper and lower bounds on frequencies of structures with interval parameters, *Mechanics Research Communications* 22 (5) (1995) 431–439.

[8] A. Dimarogonas, Interval analysis of vibrating systems, *Journal of Sound and Vibration* 183 (4) (1995) 739–749.

[9] S. Rao, P. Sawyer, Fuzzy finite element approach for the analysis of imprecisely defined systems, *AIAA Journal* 33 (12) (1995) 2364–2370.

[10] L. Chen, S. Rao, Fuzzy finite-element approach for the vibration analysis of imprecisely-defined systems, *Finite Elements in Analysis and Design* 27 (1997) 69–83.

[11] R. Muhanna, R. Mullen, Formulation of fuzzy finite-element methods for solid mechanics problems, *Computer-Aided Civil and Infrastructure Engineering* 14 (2) (1999) 107–117.

[12] D. Moens, D. Vandepitte, Fuzzy finite element method for frequency response function analysis of uncertain structures, *AIAA Journal* 40 (1) (2002) 126–136.

[13] L. Zadeh, Fuzzy sets, *Information and Control* 8 (1965) 338–353.

[14] L. Zadeh, Concept of a linguistic variable and its application to approximate reasoning .1, *Information Sciences* 8 (3) (1975) 199–249.

[15] D. Moens, D. Vandepitte, An interval finite element approach for the calculation of envelope frequency response functions, *International Journal for Numerical Methods in Engineering* 61 (14) (2004) 2480–2507.
[16] S. Laveuve, Definition einer kahan-arithmetik und ihre implementierung, *Interval Mathematics 1975*, *Lecture Notes in Computer Science* 29 (1975) 236–245.
[17] D. Moens, A Non-Probabilistic Finite Element Approach for Structural Dynamic Analysis with Uncertain Parameters, Ph.D Thesis, K.U.Leuven, Leuven, 2002.